

RESEARCH ARTICLE SUMMARY

MOLECULAR MAGNETS

A linear cobalt(II) complex with maximal orbital angular momentum from a non-Aufbau ground state

Philip C. Bunting, Mihail Atanasov, Emil Damgaard-Møller, Mauro Perfetti, Iris Crassee, Milan Orlita, Jacob Overgaard, Joris van Slageren, Frank Neese, Jeffrey R. Long*

INTRODUCTION: The magnetic properties of a single metal center are determined by a combination of its total spin S and orbital angular momentum L . Orbital angular momentum gives rise to magnetic anisotropy, an essential property for applications such as information storage and high-coercivity magnets. Unquenched L arises from an odd number of electrons in degenerate orbitals and is typically observed only for free ions, as well as for complexes of the f elements. For the majority of transition metal ions, however, orbital angular momentum is quenched by the ligand field, which removes the requisite orbital degeneracies. Maximal L for a transition metal ($L = 3$) would require an odd number of electrons in two sets

of degenerate orbitals. Such a species would entail a non-Aufbau configuration, wherein the electrons do not fill the d orbitals in the usual order of lowest to highest in energy, and likely exhibit a large magnetic anisotropy.

RATIONALE: Previous efforts have identified the utility of linear coordination environments for isolating iron complexes with unquenched orbital angular momentum and large magnetic anisotropies. Crucially, transition metals in this environment are unaffected by Jahn-Teller distortions that would otherwise remove orbital degeneracies in the case of partially filled d orbitals. Separately, cobalt atoms deposited on a MgO surface—for which

one-coordination of the metal is achieved, provided a vacuum is maintained—were shown to have $L = 3$, giving rise to near-maximal magnetic anisotropy. Calculations on the hypothetical linear molecule $\text{Co}(\text{C}(\text{SiMe}_3)_3)_2$ (where Me is methyl) also predicted that this system would possess a ground state with $L = 3$. Empirically, maximal L in a transition metal complex thus requires both a linear coordination environment and a sufficiently weak ligand field strength to allow for non-Aufbau electron filling.

RESULTS: The strongly reducing nature of the carbanion ligand hinders isolation of dialkyl cobalt(II) complexes. However, reducing the basicity of the central carbanion through the use of electron-withdrawing aryloxy groups allowed for the synthesis of the dialkyl cobalt(II) complex $\text{Co}(\text{C}(\text{SiMe}_2\text{ONaph})_3)_2$, where Naph

ON OUR WEBSITE

Read the full article at <http://dx.doi.org/10.1126/science.aat7319>

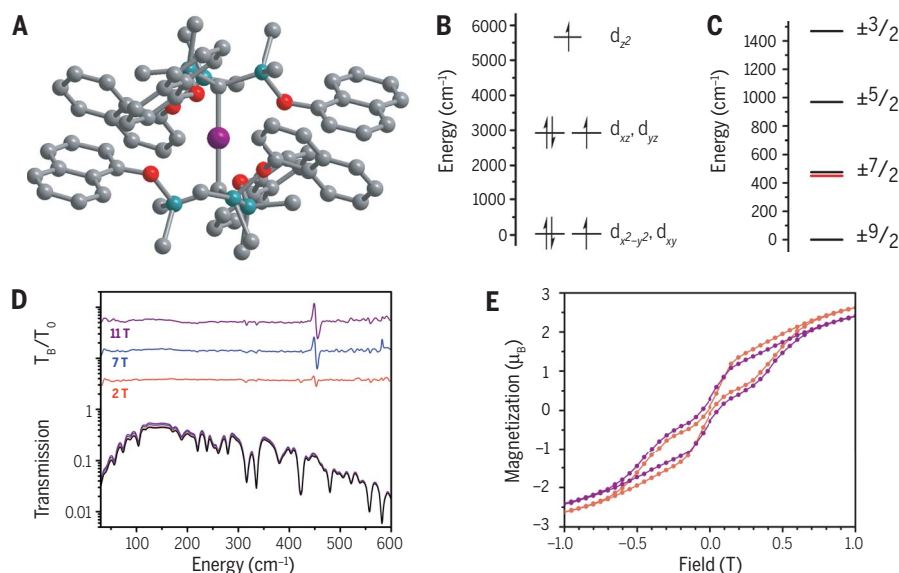
is a naphthyl group. Ab initio calculations on this complex predict a ground state with $S = 3/2$, $L = 3$, and $J = 9/2$ arising from the non-Aufbau electron configuration $(d_{xz}^2, d_{yz})^3(d_{z^2})^1$. Much as for lanthanide complexes, the ligand field is sufficiently weak that interelectron repulsion and spin-orbit coupling play the key roles in determining the electronic ground state. dc magnetic susceptibility measurements reveal a well-isolated $M_J = \pm 9/2$ ground state, and simulations of the magnetic data from the calculations are in good agreement with the experimental data. Variable-field far-infrared (FIR) spectroscopy shows a magnetically active excited state at 450 cm^{-1} that, in combination with calculations and variable-temperature ac magnetic susceptibility experiments, is assigned to the $M_J = \pm 7/2$ state. Modeling of experimental charge density maps also suggests a d -orbital filling with equally occupied $(d_{x^2-y^2}, d_{xy})$, and (d_{xz}, d_{yz}) orbital sets. As a consequence of its large orbital angular momentum, the molecule exhibits slow magnetic relaxation and, in a magnetically dilute sample, a coercive field of 600 Oe at 1.8 K.

CONCLUSION: Isolation of $\text{Co}(\text{C}(\text{SiMe}_2\text{ONaph})_3)_2$ illustrates how an extreme coordination environment can confer an f -element-like electronic structure on a transition metal complex. The non-Aufbau ground state enables realization of maximal orbital angular momentum and magnetic anisotropy near the physical limit for a $3d$ metal. In this respect, the linear L-Co-L motif may prove useful in the design of new materials with high magnetic coercivity. ■

The list of author affiliations is available in the full article online.

*Corresponding author. Email: jrlong@berkeley.edu

Cite this article as P. C. Bunting et al., *Science* **362**, eaat7319 (2018). DOI: 10.1126/science.aat7319



Linear dialkyl cobalt(II). (A) Molecular structure of $\text{Co}(\text{C}(\text{SiMe}_2\text{ONaph})_3)_2$. Purple, gray, turquoise, and red spheres represent Co, C, Si, and O, respectively. Hydrogen atoms have been omitted for clarity. (B) Energy diagram depicting the energy and electron occupations of the $3d$ orbitals. (C) The calculated splitting of the ground $^4\Phi$ state by spin-orbit coupling. The red line is the experimentally determined energy of the $M_J = \pm 7/2$ state. (D) Variable-field FIR spectra of $\text{Co}(\text{C}(\text{SiMe}_2\text{ONaph})_3)_2$. The top section shows the applied-field spectra (T_B) divided by the zero-field spectrum (T_0). (E) Variable-field magnetization data for $\text{Co}(\text{C}(\text{SiMe}_2\text{ONaph})_3)_2$ and $\text{Co}_{0.02}\text{Zn}_{0.98}(\text{C}(\text{SiMe}_2\text{ONaph})_3)_2$ at 1.8 K. μ_B , bohr magnetons.

RESEARCH ARTICLE

MOLECULAR MAGNETS

A linear cobalt(II) complex with maximal orbital angular momentum from a non-Aufbau ground state

Philip C. Bunting¹, Mihail Atanasov^{2,3}, Emil Damgaard-Møller⁴, Mauro Perfetti⁵, Iris Crassee⁶, Milan Orlita^{6,7}, Jacob Overgaard⁴, Joris van Slageren⁵, Frank Neese², Jeffrey R. Long^{1,8,9*}

Orbital angular momentum is a prerequisite for magnetic anisotropy, although in transition metal complexes it is typically quenched by the ligand field. By reducing the basicity of the carbon donor atoms in a pair of alkyl ligands, we synthesized a cobalt(II) dialkyl complex, $\text{Co}(\text{C}(\text{SiMe}_2\text{ONaph})_3)_2$ (where Me is methyl and Naph is a naphthyl group), wherein the ligand field is sufficiently weak that interelectron repulsion and spin-orbit coupling play a dominant role in determining the electronic ground state. Assignment of a non-Aufbau $(d_{x^2-y^2}, d_{xy})^3(d_{xz}, d_{yz})^3(d_{z^2})^1$ electron configuration is supported by dc magnetic susceptibility data, experimental charge density maps, and ab initio calculations. Variable-field far-infrared spectroscopy and ac magnetic susceptibility measurements further reveal slow magnetic relaxation via a 450-wave number magnetic excited state.

All materials exhibiting a large magnetic anisotropy have nonzero orbital angular momentum L arising from an electronic structure of partially filled (but not half-filled) energetically degenerate orbitals. In trivalent lanthanide ions, the valence 4f orbitals are well-shielded and interact little with their coordination environment, allowing for a nonzero L that couples with the total spin S to give rise to a total angular momentum J of $|L - S| \leq J \leq |L + S|$ and potentially a large magnetic anisotropy. In the case of transition metals, however, the ligand field typically removes any orbital degeneracy, leading to quenching of the orbital angular momentum ($L = 0$) and an appropriate description of the ground state in terms of S only. When magnetic anisotropy is present in such complexes, it is generally a weak effect that arises from mixing of electronic ground and excited states induced by spin-orbit coupling.

Creating unquenched orbital angular momentum in molecular transition metal-based systems requires an unusually weak ligand field and/or two or more orbitals that are nearly degenerate. In this context, perhaps the simplest experimental system is a one-coordinate cobalt atom: individual cobalt atoms on a MgO surface (referred to as adatoms) were recently shown by scanning probe microscopy to have a $J = 9/2$ ($L = 3, S = 3/2$) ground state and exhibit near-maximal magnetic anisotropy in a half-integer spin 3d system (1).

In the regime of molecules, complexes with linearly coordinated transition metal ions have garnered interest of late because they are energetically unaffected by Jahn-Teller distortions, allowing for the possibility of virtually unquenched orbital angular momentum (2). Analogously to lanthanide complexes, such transition metal systems with nonzero L are best described by a total angular momentum J , which is split by spin-orbit coupling and the ligand field into $2J + 1$ M_J states (where M_J is the projection of J along the magnetic axis). Two transition metal complexes that have been described by using this formalism are the iron(II) complex $\text{Fe}(\text{C}(\text{SiMe}_3)_3)_2$ (where Me is methyl) and the iron(I) complex $[\text{Fe}(\text{C}(\text{SiMe}_3)_3)_2]^-$ (3, 4). Both complexes have ground states with $L = 2$ due to electronic configurations that place three electrons in the degenerate orbital pair $d_{x^2-y^2}$ and d_{xy} , which arise from linear combinations of the d orbitals with magnetic quantum number $m_l = \pm 2$. A notable consequence of these electronic structures is that both complexes exhibit relatively large energy separations between their ground and first excited M_J states, making them prone to single-molecule

magnet behavior (5). ac magnetic susceptibility data revealed that both molecules exhibit slow magnetic relaxation (the former complex under an applied dc field and the latter in zero applied field) with effective spin-reversal barriers (U_{eff}) of 178 and 246 cm^{-1} , respectively (6)—values close to the calculated energy separations between their ground and first excited M_J states (7, 8).

At first glance it may seem impossible to increase orbital angular momentum for a transition metal complex beyond $L = 2$. An $L = 3$ ground state requires two sets of degenerate orbitals, $(d_{x^2-y^2}, d_{xy})$ ($m_l = \pm 2$) and (d_{xz}, d_{yz}) ($m_l = \pm 1$), with an odd number of electrons in each. The Aufbau principle describes the manner in which electrons fill orbitals, typically from lowest to highest energy. A more rigorous consideration of electronic structure accounts for three main effects: ligand field stabilization, interelectron repulsion, and spin-orbit coupling. Ligand field effects typically dominate when considering transition metal complexes. When the ligand field stabilization and interelectron repulsion energies are similar in transition metal complexes, high-spin electronic configurations arise. For example, placing three electrons in the orbitals $(d_{x^2-y^2}, d_{xy})(d_{xz}, d_{yz})$ could give the low-spin configuration $(d_{x^2-y^2}, d_{xy})^3(d_{xz}, d_{yz})^0$ if the energy separation between orbital pairs is larger than the electron pairing energy, or the high-spin configuration $(d_{x^2-y^2}, d_{xy})^2(d_{xz}, d_{yz})^1$ if the orbital pairs are relatively close in energy. For six electrons, the expected Aufbau filling of these orbitals is $(d_{x^2-y^2}, d_{xy})^4(d_{xz}, d_{yz})^2$, and as the sixth electron must be paired in either orbital pair, there is no reason to assume there would be any stabilization from the non-Aufbau configuration, $(d_{x^2-y^2}, d_{xy})^3(d_{xz}, d_{yz})^3$.

Calculations on the hypothetical complex $\text{Co}(\text{C}(\text{SiMe}_3)_3)_2$ show a ground state with $L = 3$, which arises from a non-Aufbau 3d-orbital filling of $(d_{x^2-y^2}, d_{xy})^3(d_{xz}, d_{yz})^3(d_{z^2})^1$, and further predict a splitting between ground and first excited M_J states of 454 cm^{-1} (9). Efforts to synthesize this molecule both by our laboratory and by others (10) were unsuccessful. Moreover, although nearly 70 two-coordinate, paramagnetic transition metal complexes have been synthesized (11), the only such compounds with alkyl ligands are of the type $[\text{M}(\text{C}(\text{SiMe}_3)_3)_2]^{0/1-}$, where M is Fe(II) (12), Fe(I) (4), Mn(II) (13), and Mn(I) (14). Several approximately linear cobalt(II) complexes have been studied, however, and one such molecule, $(\text{siPr})\text{CoNDmp}$ (where siPr is an N-heterocyclic carbene and NDmp is an arylimido ligand), has a spin-reversal barrier of 413 cm^{-1} , more than 1.5 times that measured for $[\text{Fe}^{\text{I}}(\text{C}(\text{SiMe}_3)_3)_2]^-$, despite both molecules having the same total angular momentum of $J = 7/2$ (15). Correspondingly, the increase in magnetic anisotropy for the Co(II) complex must arise from an increase in the spin-orbit coupling constant, a value which trends with effective nuclear charge. In another example, bent $[\text{CoO}]^-$ anions inserted into the channels of an apatite-type structure were shown to have a spin-reversal barrier of 387 cm^{-1} (16). A semi-empirical model

¹Department of Chemistry, University of California, Berkeley, CA 94720, USA. ²Max-Planck-Institut für Kohlenforschung, Mülheim an der Ruhr D-45470, Germany. ³Institute of General and Inorganic Chemistry, Bulgarian Academy of Sciences, Academy Georgi Bontchev, Sofia 1113, Bulgaria. ⁴Department of Chemistry and Centre for Materials Crystallography, Aarhus University, DK-8000 Aarhus C, Denmark. ⁵Institut für Physikalische Chemie and Center for Integrated Quantum Science and Technology (IQST), Universität Stuttgart, Pfaffenwaldring 55, 70569 Stuttgart, Germany. ⁶Laboratoire National des Champs Magnétiques Intenses, CNRS-UGA-UPS-INS-EMFL, 25 rue des Martyrs, 38042 Grenoble, France. ⁷Institute of Physics, Charles University, Ke Karlovu 5, 12116 Praha 2, Czech Republic. ⁸Department of Chemical and Biomolecular Engineering, University of California, Berkeley, CA 94720, USA. ⁹Materials Sciences Division, Lawrence Berkeley National Laboratory, Berkeley, CA 94720, USA.

*Corresponding author. Email: jrlong@berkeley.edu

based on ligand field parameterization predicted that such a barrier could arise from a $J = 9/2$ ground state, with increasing mixing of M_J states (and a concomitant diminishing of the barrier height) arising as the $[\text{OCoO}]^-$ anion becomes increasingly bent. In the extreme case of the cobalt adatoms mentioned above, a separation of 468 cm^{-1} was determined for the separation between $M_J = 9/2$ and $7/2$ states (**1**).

Our motivations to isolate a dialkyl cobalt(II) complex were thus twofold: First, the proposed electronic structure violates the Aufbau principle and is analogous to what is commonly seen for lanthanides; second, realizing maximal orbital angular momentum should afford a very large magnetic anisotropy, a property that has important applications in the study of magnetism. Here, we present the synthesis and characterization of such a dialkyl cobalt(II) complex and confirm the proposed $J = 9/2$ ground state through direct electronic and spectroscopic measurements, ab initio modeling, and magnetic susceptibility measurements. The energy separation between the $M_J = \pm 9/2$ and $\pm 7/2$ states leads to slow magnetic relaxation at temperatures as high as 70 K and low-temperature magnetic hysteresis.

Synthesis and structure of a linear cobalt dialkyl complex

Our attempts to synthesize $\text{Co}(\text{C}(\text{SiMe}_3)_3)_2$ from metathesis reactions of $[\text{C}(\text{SiMe}_3)_3]^-$ salts and CoX_2 ($\text{X} = \text{Cl}, \text{Br}, \text{or I}$) gave only intractable amorphous black solids. Similar reactivity with $[\text{C}(\text{SiMe}_3)_3]^-$ was reported previously, but after switching to $[\text{C}(\text{SiMe}_2\text{Ph})_3]^-$ (where Ph is phenyl), we found it possible to isolate the dimer $[\text{Co}(\text{C}(\text{SiMe}_2\text{Ph})_3)_2]$, a product formed by the in situ reduction of cobalt(II) (**10**). Thus, at least one challenge in isolating a dialkyl cobalt(II) complex is the strongly reducing nature of the carbanion. Others have shown that substituting electron-withdrawing alkoxides onto each silyl group substantially reduces the basicity and electron density of the carbanion (**17, 18**). In an initial pursuit of this approach, we found that $[\text{C}(\text{SiMe}_2\text{OPh})_3]^-$ did support a dialkyl cobalt(II) complex, $\text{Co}(\text{C}(\text{SiMe}_2\text{OPh})_3)_2$, but long-range $\text{Co}\cdots\text{O}$ interactions led to a substantially bent C–Co–C axis (fig. S1). We next synthesized a number of $[\text{C}(\text{SiMe}_2\text{OR})_3]^-$ derivatives ($\text{R} =$ various alkyl or substituted phenyl groups) by following the general reaction scheme outlined in Fig. 1A. Smaller substituents did not readily yield isolable products, and larger substituents supported only dinuclear complexes of the type $(\text{R}_3\text{CCo})_2(\mu\text{-X})_2$ (where X is a halide), similar to the structure of $(\text{PhMe}_2\text{Si})_3\text{CZn}(\mu\text{-Cl})_2$ (**19**). In an effort to reduce the nucleophilicity of the oxygen atom, we also tried using electron-withdrawing substituents such as perfluorophenyl but found these ligands to be susceptible to Si–O cleavage, a challenge also encountered in trying to metalate other $\text{HC}(\text{SiMe}_2\text{OR})_3$ complexes with MeLi (**20**). Ultimately, we determined that only the naphthol ($\text{R} = \text{Naph} = \text{C}_{10}\text{H}_7$) derivative yielded the requisite linear geometry.

The reaction of two equivalents of $\text{KC}(\text{SiMe}_2\text{ONaph})_3$ with CoBr_2 in tetrahydrofuran (THF) at 60°C affords a green solution. After removal of the solvent in vacuo and redissolution into hexanes, dark red crystals of $\text{Co}(\text{C}(\text{SiMe}_2\text{ONaph})_3)_2$ (**1**) emerged from the green solution over the course of several days at room temperature. Crystallization at -30°C formed green crystals that were not suitable for x-ray diffraction, but elemental analysis of the thoroughly dried crystals suggested the isolation of the solvated complex, $\text{Co}(\text{C}(\text{SiMe}_2\text{ONaph})_3)_2(\text{THF})$. Compound **1** is insoluble in common organic solvents, and exposure to THF led to the formation of a green solution that is likely the aforementioned solvated complex. The zinc congener, $\text{Zn}(\text{C}(\text{SiMe}_2\text{ONaph})_3)_2$ (**2**), was obtained from the reaction of $\text{KC}(\text{SiMe}_2\text{ONaph})_3$ and ZnBr_2 in Et_2O ($\text{Et} = \text{ethyl}$). After removal of KBr by filtration, colorless crystals of **2** grew from the Et_2O solution over the course of several days. Using the same reaction conditions with a mixture of ZnBr_2 and $\text{CoBr}_2(\text{THF})$ further enabled the preparation of a magnetically dilute sample, $\text{Co}_{0.02}\text{Zn}_{0.98}(\text{C}(\text{SiMe}_2\text{ONaph})_3)_2$ (**3**).

Single-crystal x-ray diffraction analysis revealed compounds **1** and **2** to be isostructural, crystallizing in space group $R\bar{3}$ (no. 148) and featuring a

linear C–M–C axis imposed by the S_6 site symmetry (Fig. 1, B and C). The Co–C and Zn–C interatomic distances of 2.066(2) and 1.995(3) Å, respectively, are similar to the Fe–C separation of 2.0505(14) Å in $\text{Fe}(\text{C}(\text{SiMe}_3)_3)_2$ (**12**) and the Zn–C separation of 1.982(2) Å in $\text{Zn}(\text{C}(\text{SiMe}_3)_3)_2$ (**21**). In addition, the $\text{Co}\cdots\text{O}$ distance of 3.1051(11) Å and the $\text{Zn}\cdots\text{O}$ distance of 3.1240(16) Å are substantially longer than the sum of cobalt or zinc and oxygen ionic radii (~ 2.2 Å), suggesting minimal interactions. Instead, the staggered orientation of the ligands facilitates close $\text{sp}^3\text{-CH}\cdots\pi$ and $\text{sp}^2\text{-CH}\cdots\pi$ contacts of 2.692 and 2.822 Å, respectively (fig. S3), which are in the range of weak $\text{CH}\cdots\pi$ interactions (**22**). This suggests that interligand interactions may help stabilize **1**, consistent with reports of dispersion forces stabilizing other two-coordinate complexes (**23**).

Electronic structure calculations

Ab initio calculations performed on **1** by using the crystal structure geometry reveal that the ^4F free-ion state is split by the linear ligand field into three doubly-degenerate states, $^4\Phi$, $^4\Pi$, and $^4\Delta$, and one nondegenerate state, $^4\Sigma^-$ (here we employ $C_{\infty v}$ point group notation). Because of the weak ligand field, the seven states of ^4F parentage are split by less than 3000 cm^{-1}

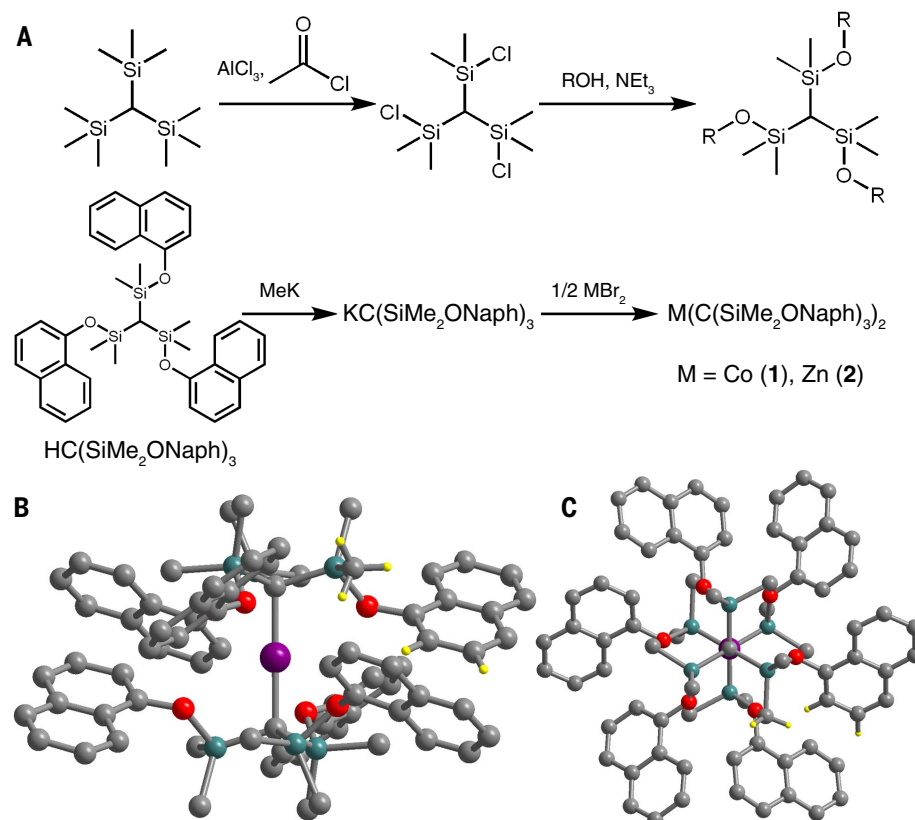


Fig. 1. Synthesis and structure of linear Co and Zn dialkyl complexes. (A) General synthetic scheme for ligands of the type $\text{HC}(\text{SiMe}_2\text{OR})_3$ and synthesis of compounds **1** and **2**. **(B)** Molecular structure of $\text{Co}(\text{C}(\text{SiMe}_2\text{ONaph})_3)_2$ (**1**). Purple, gray, turquoise, red, and yellow spheres represent Co, C, Si, O, and H atoms, respectively. Most hydrogen atoms have been omitted for clarity. Hydrogen atoms are shown on three carbons to illustrate the location of the $\text{CH}\cdots\pi$ interactions. **(C)** Molecular structure of $\text{Co}(\text{C}(\text{SiMe}_2\text{ONaph})_3)_2$ viewed along the molecular z axis.

(accounting also for interelectron repulsion energy). This splitting is small even relative to that of other two-coordinate complexes; for example, the ^5D and ^4F free-ion states of $\text{Fe}(\text{C}(\text{SiMe}_3)_3)_2$ and $[\text{Fe}(\text{C}(\text{SiMe}_3)_3)_2]^-$ are split by 5000 and 6000 cm^{-1} , respectively (3, 4, 7). Excitations from the $^4\Phi$ ground state of **1** to the $^4\Sigma^-(^4\text{P})$ and $^4\text{Ti}(^4\text{P})$ states were calculated to be spectroscopically accessible at 13,537 and 18,864 cm^{-1} and are observed in the ultraviolet-visible (UV-vis) diffuse reflectance spectrum at 12,000 and 15,000 cm^{-1} (fig. S4). The splitting of the $^4\Phi$ ground state due to spin-orbit coupling results in four sets of Kramers doublets, best described by $M_J = \pm 9/2$, $\pm 7/2$, $\pm 5/2$, and $\pm 3/2$, in order of increasing energy. The total splitting of $^4\Phi$ is 1469 cm^{-1} , whereas the calculated separation between just $M_J = \pm 9/2$ and $M_J = \pm 7/2$ is 476 cm^{-1} . Additional calculations performed on a truncated model molecule show that inclusion of the carbon σ -bonding electrons in the complete active space has only a very minor effect (less than 3%) on the energies of both the nonrelativistic and relativistic states (tables S10 and S11).

Ligand field analysis of the calculations revealed the $^4\Phi$ ground state to have the 3d-orbital filling $(d_{x^2-y^2}, d_{xy})^3(d_{xz}, d_{yz})^3(d_{z^2})^1$ (Fig. 2A), which deviates from the expected Aufbau orbital filling of $(d_{x^2-y^2}, d_{xy})^4(d_{xz}, d_{yz})^2(d_{z^2})^1$ ($^4\Sigma^-$) and can be explained by considering the competing effects of ligand-field stabilization and interelectron repulsion. In general, interelectronic repulsion is strongest for two electrons occupying the same orbital (necessarily with opposite spin). Two electrons with opposite spin in different orbitals alternatively experience medium-strong electron-electron repulsion, whereas two electrons with parallel spin (necessarily in different orbitals) repel each other least strongly, owing to the presence of the Fermi hole. Typically, only

the electron-pairing energy component of interelectron repulsion is important for transition metal complexes, and whether a complex is high or low spin is determined by considering whether the ligand field strength is small or large compared with the pairing energy. In the case of **1**, the ligand field strength is so small that not only does the molecule display a high-spin state, but it also maximizes its orbital angular momentum in keeping with the Hund rule for free atoms and ions, thus leading to a non-Aufbau ground state configuration. Clearly, the $(d_{x^2-y^2}, d_{xy})^3(d_{xz}, d_{yz})^3(d_{z^2})^1$ configuration minimizes electron-electron repulsion relative to the alternative $(d_{x^2-y^2}, d_{xy})^4(d_{xz}, d_{yz})^2(d_{z^2})^1$ configuration that features an electronically crowded $(d_{x^2-y^2}, d_{xy})^4$ subshell. This stabilization is also reflected in the total orbital angular momentum of the ground state that is an approximately good quantum number in this system. Nonrelativistic ligand field calculations without interelectron repulsion show the expected ground state of $^4\Sigma^-$ (with $L = 0$). By using ligand field parameters from ab initio n -electron valence perturbation theory to second order (NEVPT2) calculations and ligand field expressions for the $S = 3/2$ states under linear symmetry with interelectron repulsion, the high orbital angular momentum $^4\Phi$ state (with $L = 3$) is stabilized by 1300 cm^{-1} relative to the $^4\Sigma^-$ state (Fig. 2B and table S9). Spin-orbit coupling further stabilizes the $M_J = 9/2$ component of the $^4\Phi$ ground state by 788 cm^{-1} .

This situation is completely distinct from that of established complexes with stronger ligand fields that can sometimes have electronic ground states with substantial contributions from non-Aufbau configurations. For example, the iron(II) metallophthalocyanine complex (FePc) has a ground state with nearly equal contributions from Aufbau and non-Aufbau configurations,

wherein the non-Aufbau component arises from an accidental orbital near-degeneracy (24). The essential difference between complex **1** and FePc, however, is in ligand field strength, with the two molecules calculated to exhibit total d-orbital splittings of 6000 and 165,000 cm^{-1} (24), respectively. With the focus on the orbitals that give rise to the non-Aufbau states, the $(d_{x^2-y^2}, d_{xy})$ and (d_{xz}, d_{yz}) orbital pairs are separated by 2900 cm^{-1} in **1**, whereas for FePc the (d_{xz}, d_{yz}) orbital pair and d_{z^2} orbital are separated by 19,000 cm^{-1} (24). Our calculations show that interelectron repulsion in **1** easily overwhelms the ligand field stabilization energy associated with the Aufbau configuration, destabilizing the $^4\Sigma^-(^4\text{P})$ state by 12,000 cm^{-1} relative to the $^4\Phi$ state. No similar calculations appear to have been reported for FePc, but it is clear that it would be impossible to observe a pure non-Aufbau ground state as long as the ligand field stabilization energy is of the same magnitude as interelectron repulsion. Once the ligand field requirement for a non-Aufbau ground state is met, it is also possible to observe maximal orbital angular momentum. The maximal orbital angular momentum of $L = 3$ for transition metals requires degenerate $(d_{x^2-y^2}, d_{xy})$ and (d_{xz}, d_{yz}) orbital pairs, and thus the molecule should also be linear to avoid Jahn-Teller distortions.

The ligand field analysis elucidates another challenge in isolating a dialkyl cobalt complex: Namely, the ligand field stabilization energy suggests that metal-ligand bond formation provides only a minor stabilizing effect of 4.8 kcal/mol (1700 cm^{-1}). This result is perhaps intuitively understood by considering that the formal Co-C bond order is approximately one-half, because the (d_{xz}, d_{yz}) orbitals have slight π -antibonding character and are destabilized primarily by electrostatic interactions. It is not until we consider transmetallic dispersion and electrostatic ($\text{CH}\cdots\pi$) forces that **1** appears to be stable.

Charge density determination

The molecular charge density (CD) of **1** was obtained from multipolar refinement of single-crystal x-ray diffraction data measured at 20 K by using synchrotron radiation. A small amount of disorder (~6%) is present in the structure because of flipping of the naphthalene groups (also involving the O and Si atoms); however, a detailed description of this disorder was possible and allowed us to extract quantitative information pertinent to the magnetic properties (see methods for a detailed description of the experimental procedure).

The experimental temperature of 20 K is low enough that the CD represents primarily the electronic properties of the relativistic ground state. We used an atom-centered multipole formalism to describe the CD, and thus a complete set of spherical harmonic functions for each atom was used to quantify the deviations from a spherical density distribution. The use of this formalism enables estimation of 3d-orbital populations on the central cobalt atom, under the assumption that the density around the metal

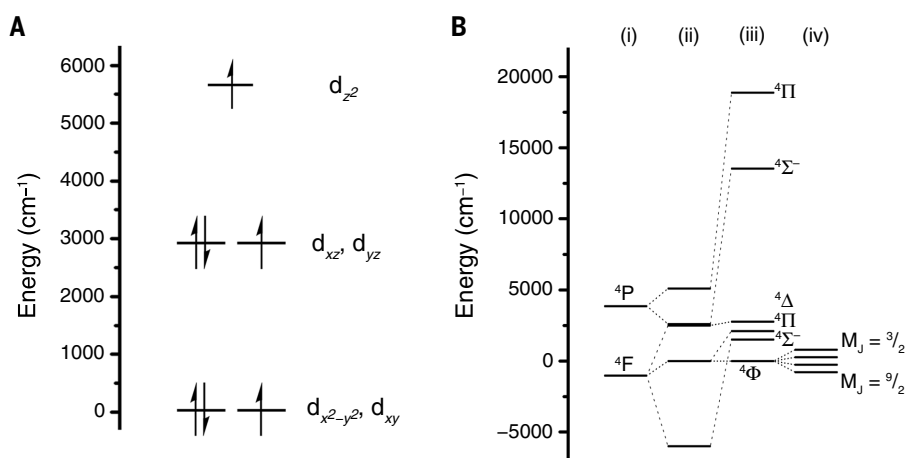


Fig. 2. Electronic structure analysis. (A) Energy diagram depicting the energy and electron occupations of the 3d orbitals on the basis of ligand field analysis of ab initio calculations. (B) Electronic structure of (i) a free Co(II) ion, (ii) $\text{Co}(\text{C}(\text{SiMe}_2\text{ONaph})_3)_2$ (**1**) considering only ligand field interactions, (iii) $\text{Co}(\text{C}(\text{SiMe}_2\text{ONaph})_3)_2$ considering both ligand field interactions and interelectron repulsion, and (iv) the splitting of the ground $^4\Phi$ state of $\text{Co}(\text{C}(\text{SiMe}_2\text{ONaph})_3)_2$ because of spin-orbit coupling according to ab initio calculations. Term symbols are for $C_{\infty v}$ symmetry. The splitting between the ground $M_J = 9/2$ and maximal excited $M_J = 3/2$ states is 1469 cm^{-1} .

originates solely from the atom itself (i.e., that no substantial covalent bonding occurs). The parameterized CD also enables an analysis in the framework of quantum theory of atoms in molecules (QTAIM) (25) and estimates of atomic charges and the strength of chemical bonding. With the local coordination axes defined such that the Co–C direction is along the z axis, the electron density of the cobalt valence shell is distributed in the following manner: 42.8% is in the $(d_{x^2-y^2})$ orbitals, 41.2% is in the (d_{xz}, d_{yz}) orbitals, and 16.0% is in the d_{z^2} orbital. Furthermore, the same distribution of electrons in the cobalt 3d orbitals was obtained regardless of the manner in which the naphthalene disorder was treated.

Variable-field far-infrared spectroscopy

We sought to confirm experimentally the magnitude of the separation between the ground and first excited magnetic states in **1** by using variable-field far-infrared (FIR) spectroscopy (26, 27). Although such energy separations are more commonly determined by fitting low-temperature magnetization data or high-temperature magnetic relaxation data, these approaches give values that are sensitive to fitting procedures and provide only an indirect measure of the representative ground-to-excited-state energy separation. Additionally, given the calculated energy splitting of 476 cm^{-1} for the lowest M_J states, dc susceptibility measurements would provide limited information on the position of excited states, as the Boltzmann population of the ground state doublet is still 90% at 300 K. Thus, not only is spectroscopy a more direct measurement, but in this case, it is also necessary to gain information on the excited states. Transmission spectra in the 30- to 600-cm^{-1} energy range were collected at a temperature of 4.2 K under applied fields ranging from 0 to 11 T (Fig. 3A). Although absorption bands associated with magnetic dipole transitions are usually substantially weaker than those of electronic dipole transitions, a pronounced field dependence is immediately evident in the data upon dividing the applied-field spectra by the zero-field spectrum (Fig. 3B). The only peak visible in this energy range is at 450 cm^{-1} and is attributable to the transition from $M_J = \pm 9/2$ to $\pm 7/2$, in good agreement with the calculated separation of 476 cm^{-1} . A steadily increasing blue shift of the infrared (IR) absorption maximum is observed with increasing applied fields (fig. S5) and is in good agreement with a simulation of the spectral envelope magnetic dipole $M_J = \pm 9/2$ to $\pm 7/2$ transitions (fig. S6). In addition to the blue shift, there is a concomitant decrease in absorption intensity and peak broadening with increasing field, giving rise to the derivative shape observed in Fig. 3B.

Magnetic properties

Variable-temperature dc magnetic susceptibility data for **1** are shown in Fig. 4A. The gradual decrease in the product of the molar magnetic susceptibility and temperature ($\chi_M T$) with de-

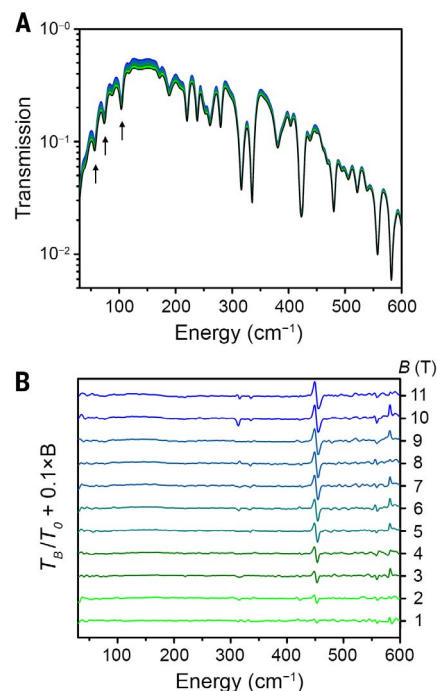


Fig. 3. Variable-field FIR spectroscopy.

(A) Absolute transmission spectra for **1** collected at 4.2 K under applied fields ranging from 0 to 11 T. Phonon energies used in Eq. 2 to describe magnetic relaxation are marked with arrows. (B) Plots of applied-field spectra (T_B) divided by the zero-field spectrum (T_0), where B is the applied field. The peak at 450 cm^{-1} corresponds to the transition from $M_J = 9/2$ to $M_J = 7/2$. The spectra have been vertically offset for clarity.

creasing temperature is indicative of magnetic anisotropy, whereas the strong field dependence at low temperature arises from an increased Zeeman splitting at higher fields. The room temperature $\chi_M T$ value of $4.89\text{ cm}^3\text{ K mol}^{-1}$ is consistent with a well-isolated $M_J = 9/2$ ground state (the theoretical $\chi_M T$ value for an isotropic $J = 9/2$ ion is $5.47\text{ cm}^3\text{ K mol}^{-1}$), and reduced magnetization plots (Fig. 4B) show a saturation magnetization of 3.00 bohr magnetons (μ_B). The simulated $\chi_M T$ and reduced magnetization data from ab initio calculations (solid lines, Fig. 4) are in close agreement with the experimental data, further corroborating the well-isolated $M_J = 9/2$ ground state.

ac susceptometry was used to probe magnetic relaxation in the range from 10^{-4} to 10^1 s (10^5 to 10^{-1} Hz). By fitting the in-phase (χ') and out-of-phase (χ'') susceptibility (figs. S8 to S11) to a generalized Debye model, we obtained relaxation times for **1**, as shown in the Arrhenius plot in Fig. 5A. The temperature dependence of the magnetic relaxation time (τ) in molecules exhibiting slow magnetic relaxation is typically described by the expression

$$\tau^{-1} = \frac{A_1}{1 + A_2 H^2} + B H^4 T + C T^n + \tau_0^{-1} \exp(-U/k_B T) \quad (1)$$

where the four terms represent quantum-tunneling, direct, Raman, and Orbach relaxation processes, respectively (28–30). However, we were unable to fit the relaxation data for **1** to the total sum of these processes. An alternative model for through-barrier relaxation has recently been proposed, wherein specific phonon modes may facilitate relaxation through direct doublet transitions (31, 32). Building on the results of Lunghi and co-workers, we derived the expression

$$\tau^{-1} = \tau_{\text{tunnel}}^{-1} + \sum_{\alpha} \left(\frac{V_{\alpha}^2}{\hbar} \frac{\Delta_{\alpha} (2n_{\alpha} + 1)}{[\Delta_{\alpha}^2 + (\hbar\omega_{\alpha})^2]} \right) + \tau_0^{-1} \exp(-U/k_B T) \quad (2)$$

where the first term represents quantum tunneling and the last term represents Orbach relaxation. The second term represents relaxation through the α -th phonon mode, V represents spin-phonon coupling, Δ is the phonon linewidth, n is the phonon occupation number, ω is the phonon frequency, and \hbar is Planck's constant. Both Δ and n are dependent on both temperature and ω . Values for U and ω are taken from the variable-field FIR data, whereas τ_{tunnel} , V , and τ_0 are fit parameters (see eqs. S1 to S4 for details). From this equation, we were able to obtain reasonable fits (SE of the estimate = 0.17 and 0.21 for **1** and **3**, respectively) to the relaxation data in Fig. 5A.

To further examine the effect of any tunneling relaxation process, we collected data under a 3000-Oe field. The lack of a temperature-independent region at low temperature under zero and applied field indicates that molecular quantum tunneling is not a dominant relaxation pathway above 4 K; however, the observed increase in relaxation times upon application of a dc field (Fig. 5A) demonstrates that it is a contributing factor. To some extent, the tunneling relaxation rate can be slowed through magnetic dilution (33), and a magnetically dilute sample prepared with a 1:49 ratio of cobalt to zinc (**3**) exhibits lower relaxation rates than **1** under zero field. The lack of a linear temperature dependence at the highest temperatures indicates that two-phonon Orbach relaxation (involving excitation to and relaxation from a real excited state) is not yet dominant at 70 K. By using the value of $U = 450\text{ cm}^{-1}$ obtained from FIR spectroscopy, however, we determined an upper bound for τ_0 of $1.79 \times 10^{-9}\text{ s}$, which is a reasonable value for a single-molecule magnet (5).

The low-temperature relaxation dynamics of **1** and **3** were also probed by using dc relaxation and magnetization experiments (Fig. 5B). The tunneling and direct relaxation terms introduced above were used in fits of the variable-field relaxation data and are discussed in detail in the methods. The relaxation times extracted at 1.8 K and zero applied field are 16.4 ± 0.7 and $48.2 \pm 4.7\text{ s}$ for **1** and **3**, respectively, and these values slow to 221 and 660 s at 1.8 K under a 1500-Oe applied field. These relaxation times suggest that magnetic hysteresis should be apparent in variable-field magnetization data, and

1 and **3** show waist-restricted hysteresis loops between -0.7 and 0.7 T up to 5 K. A sudden decline in the magnetization as the field approaches zero can be ascribed to rapid relaxation induced by tunneling of the magnetization (Fig. 5, C and D), and this decline results in small values of the remnant magnetization for **1** ($0.08 \mu_B$) and **3** ($0.28 \mu_B$) at 1.8 K that diminish to near zero at higher temperatures. Despite the relatively fast relaxation at zero field, **1** has a coercive field H_c of 180 Oe at 1.8 K, as measured with a field sweep rate of 32 Oe/s. Under the same conditions, the magnetically dilute sample, **3**, exhibits $H_c = 600$ Oe.

Outlook

These results have clear implications for technologies that require a large magnetic anisotropy. For a magnetic bit to retain its magnetization for information storage, the magnetic anisotropy energy must be substantially greater than the thermal energy. For the cobalt adatom on MgO, the separation between the ground ($M_J = \pm 9/2$) and first excited ($M_J = \pm 7/2$) states was determined to be 468 cm^{-1} , and it was suggested that this value was near a physical limit for magnetic anisotropy for 3d transition metals. This limit can be quantified by using the phenomenological spin-orbit coupling Hamiltonian, $H_{\text{SOC}} = \lambda \mathbf{L} \mathbf{S} = (\zeta/2S) \sum_i \mathbf{L}_i \mathbf{S}_i$, where λ is the effective spin-orbit coupling constant, ζ is the atomic spin-orbit coupling constant, and $\mathbf{L} = \sum_i \mathbf{L}_i$ and $\mathbf{S} = \sum_i \mathbf{S}_i$ are the operators for the orbital and spin-angular momenta, respectively (the index i sums over individual electrons). In systems with a doubly degenerate ground state, the energies (E) of the M_J states (where $M_J = M_S + M_L$) are given by $E(M_J) = (\zeta/2S) M_J M_S$; the separation between lowest and highest M_J states is equal to $L\zeta$, and the separation between adjacent states is $(L/2S)\zeta$. Thus, the actual limit for the energy separation between ground and first excited states would be found in a system with $L = 3$ and $S = 1$. However, in order to maximize relaxation times, it is advantageous to use half-integer spin systems, as the crystal field cannot couple the two components of the lowest doublet and the tunneling relaxation pathway is therefore suppressed (34). The maximal total angular momentum for a transition metal with half-integer spin is $J = 9/2$, exhibited by both the cobalt adatom and compound **1**. The magnetic M_J states of **1** span a substantial calculated energy range of 1469 cm^{-1} , and the separation between the ground ($M_J = \pm 9/2$) and first excited ($M_J = \pm 7/2$) states alone is 450 cm^{-1} . Within a rigorously linear geometry, it may be possible to further increase the magnetic anisotropy by changing the nature of the Co–L bond (L = ligand) and by increasing the spin-orbit coupling constant. However, at present the barrier of $U_{\text{eff}} = 450 \text{ cm}^{-1}$ determined here for **1** is the largest measured to date for any transition metal single-molecule magnet, with the second largest being $U_{\text{eff}} = 413 \text{ cm}^{-1}$ from the aforementioned (sIPr)CoNDmp complex (15). Given the similarity between the cobalt adatom and **1**, it is possible that this

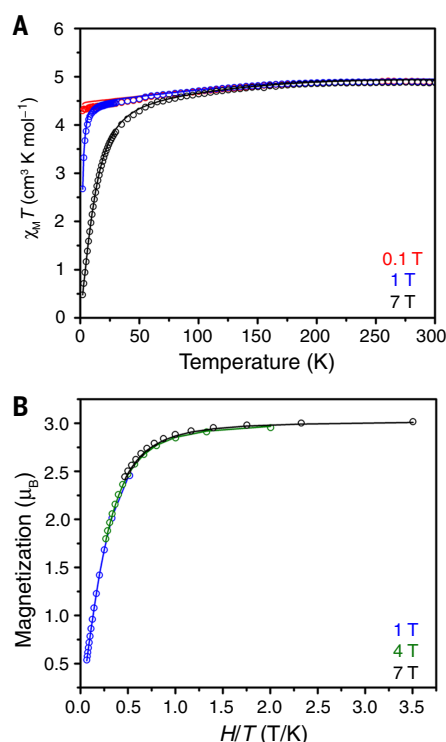


Fig. 4. Magnetic susceptibility and reduced magnetization analysis. (A) Variable-temperature molar magnetic susceptibility times temperature ($\chi_M T$) for **1** collected under dc fields (H) of 0.1 , 1 , and 7 T. Solid lines are simulated data from ab initio calculations. (B) Reduced magnetization data for **1** collected at temperatures from 2 to 15 K under dc fields of 1 , 4 , and 7 T. Solid lines are simulated data from ab initio calculations.

value is near the physical limit. Our calculations for the Co adatom on MgO indicate that the $^4\Phi(^4F)$ ground state is also well isolated in this system, suggesting that spin-orbit coupling is also the dominant factor determining the energies of the M_J states (table S13). Although information storage will certainly require longer zero-field relaxation times than observed here, magnetic relaxation times can be substantially affected by the molecular environment, as has been observed for terbium(III) bis(phthalocyaninato) molecules in bulk solids (35) and on a variety of surfaces (36–41). A comparison of the relaxation times of the cobalt adatom on MgO and those of compound **1** indicates that such an environmental effect is at play. The two cobalt centers have similar electronic structures, yet the relaxation time for the adatom at 0.6 K is on the order of 10^{-4} s, whereas a much longer relaxation time on the order of 10^1 s is observed for **1** at 1.8 K.

Beyond the implications for molecular magnetism, an intriguing potential use of the linear L–Co^{II}–L moiety is in the pursuit of lanthanide-free bulk magnets. Generally speaking, orbital angular momentum and spin-orbit coupling tie the magnetic moment to the lattice (42). In bulk magnetism, orbital angular momentum is re-

sponsible for magnetocrystalline anisotropy, the main determinant of magnetic coercivity, which is why the strongest magnets, such as $\text{Nd}_2\text{Fe}_{14}\text{B}$ and SmCo_5 , feature lanthanide ions with unquenched orbital angular momentum. Our results show how linearly coordinated transition metal ions could provide a similar effect. For example, the extended solid $\text{Li}_2(\text{Li}_{1-x}\text{Fe}_x)\text{N}$ features linear iron(I) centers similar to those in $[\text{Fe}(\text{C}(\text{SiMe}_3)_3)_2]^-$, and in high concentration ($x = 0.28$), this material displays a large coercivity ($H_c = 11.6$ T at 2 K) (43). The magnetic anisotropy of compound **1** is nearly twice as large as that of $[\text{Fe}(\text{C}(\text{SiMe}_3)_3)_2]^-$, and incorporation of the L–Co^{II}–L moiety in an extended solid could therefore in principle lead to permanent magnets with an even greater coercivity.

Materials and methods

General considerations

Unless otherwise noted, all manipulations were carried out using standard air-free Schlenk line and glove box techniques under an argon atmosphere. Reagents were purchased from commercial vendors. Anhydrous CoBr_2 and ZnBr_2 were used as received, whereas 1-naphthol was sublimed and triethylamine (NEt_3) was dried over KOH and distilled prior to use. $\text{HC}(\text{SiMe}_2\text{Cl})_3$ (17) and MeK (44) were prepared according to literature procedures. Solvents were dried by using a commercial solvent purification system designed by JC Meyer Solvent Systems. Elemental analysis was performed at the Microanalytical Laboratory of the University of California, Berkeley. Nuclear magnetic resonance (NMR) spectra were collected on a 500-MHz Bruker spectrometer; chemical shifts are reported in parts per million (ppm) referenced to residual protiated solvent.

Synthesis of $\text{HC}(\text{SiMe}_2\text{OPh})_3$ and $\text{HC}(\text{SiMe}_2\text{OC}_{10}\text{H}_7)_3$

A 100-ml Schlenk flask containing a stir bar was charged with a THF solution (50 ml) of $\text{HC}(\text{SiMe}_2\text{Cl})_3$ (3.73 g, 12.7 mmol) and NEt_3 (1.80 ml, 38.1 mmol). A separate 50-ml Schlenk flask was charged with a THF solution (25 ml) of 1-naphthol (5.58 g, 38.7 mmol). The 1-naphthol solution was added to the reaction flask over the course of several minutes with stirring, and a white precipitate immediately formed upon addition. The reaction mixture was stirred at room temperature for 3 hours, after which air-free techniques were no longer required. Water (20 ml) was added to the reaction flask, and the organic layer was collected. The water was extracted with 3×20 ml Et_2O , and the combined organic layers were dried with MgSO_4 . The ether solvent was removed under reduced pressure, leaving a colorless residue. The residue was washed with MeOH (50 ml), and the resulting white solid, $\text{HC}(\text{SiMe}_2\text{OC}_{10}\text{H}_7)_3$ (5.15 g, 66%), was collected by filtration. Anal. calcd. for $\text{C}_{37}\text{H}_{40}\text{O}_3\text{Si}_3$: C, 72.03; H, 6.54. Found: C, 72.04; H, 6.75. ^1H NMR (500 MHz, THF- d_8): δ 8.33 (3 H, d), 7.83 (3 H, d), 7.47 (3 H, d), 7.40 (6 H, m), 7.32 (3 H, t), 7.03 (3 H, d), 1.39 (1 H, s), 0.63 (18 H, s) ppm. ^{13}C NMR (500 MHz, THF- d_8): δ 151.8, 136.0, 128.9, 128.3,

126.7, 126.4, 125.7, 123.4, 122.0, 114.4, 13.1, 2.9, 2.8 ppm.

The same method was used to synthesize $\text{HC}(\text{SiMe}_2\text{OPh})_3$, which has been reported previously using a different synthetic method (45). The identity of $\text{HC}(\text{SiMe}_2\text{OPh})_3$ was confirmed by ^1H NMR spectroscopy.

Synthesis of $(\text{CH}_3\text{OCH}_2\text{CH}_2\text{OCH}_3)_2\text{KC}(\text{SiMe}_2\text{OPh})_3$

Solid MeK (0.11 g, 1.9 mmol) was slowly added to a stirring solution of **1** (0.91 g, 1.9 mmol) dissolved in Et_2O (10 ml) and dimethoxyethane (3 ml); bubbles evolved during the course of addition. The reaction mixture was then allowed to stir for 3 hours, during which time a white microcrystalline solid precipitated from solution. The solid was collected by filtration and dried under vacuum (0.65 g, 0.95 mmol, 49%). Anal. calcd. for $\text{KC}_{33}\text{H}_{53}\text{O}_7\text{Si}_3$: C, 57.85; H, 7.80. Found: C, 57.83; H, 7.60. ^1H NMR (500 MHz, THF-d8): δ 7.15 (6 H, t), 6.91 (6 H, d), 6.83 (3 H, t), 3.42 (8 H, s), 3.26 (12 H, s), 0.24 (18 H, s) ppm. ^{13}C NMR (500 MHz, THF-d8): δ 158.3, 129.7, 122.2, 121.0, 72.7, 58.9, 16.8, 15.7, 5.2 ppm.

Synthesis of $\text{KC}(\text{SiMe}_2\text{OC}_{10}\text{H}_7)_3$

$\text{HC}(\text{SiMe}_2\text{OC}_{10}\text{H}_7)_3$ (0.967 g, 1.57 mmol) was dissolved in THF (15 ml). Freshly prepared MeK (0.0850 g, 1.57 mmol) was added as a solid to the stirring reaction mixture; bubbles evolved from the mixture over the course of an hour. After 3 hours, the reaction mixture was filtered through diatomaceous earth and solvent was removed under reduced pressure, leaving a sticky colorless residue. Hexane was added to precipitate a white solid, $\text{KC}(\text{SiMe}_2\text{OC}_{10}\text{H}_7)_3$ (1.20 g, 76%), which was collected by filtration. Anal. calcd. for $\text{KC}_{37}\text{H}_{39}\text{O}_3\text{Si}_3$: C, 67.84; H, 6.00. Found: C, 67.59; H, 6.31. ^1H NMR (500 MHz, THF-d8): δ 8.42 (3 H, d), 7.71 (3 H, d), 7.49 (3 H, d), 7.28 (12 H, m), 0.38 (18 H, s) ppm. ^{13}C NMR (500 MHz, THF-d8): δ 154.8, 135.9, 129.7, 127.7, 126.9, 125.6, 124.4, 124.2, 118.7, 114.5, 16.2, 5.9, 5.8 ppm.

Synthesis of $\text{Co}(\text{C}(\text{SiMe}_2\text{OPh})_3)_2$

Solid CoCl_2 (18.2 mg, 0.140 mmol) was added to a stirring THF solution (10 ml) of $(\text{CH}_3\text{OCH}_2\text{CH}_2\text{OCH}_3)_2\text{KC}(\text{SiMe}_2\text{OPh})_3$ (200. mg, 0.290 mmol) at room temperature, and then the mixture was stirred for 2 hours at 60°C. The solvent was removed in vacuo, and the resulting blue-green solid was dissolved in hexanes. The hexanes solution was stirred at 60°C for 1 hour to form a yellow-green solution. The hexanes solution was filtered through diatomaceous earth and was concentrated in vacuo. Red-brown crystals of $\text{Co}(\text{C}(\text{SiMe}_2\text{OPh})_3)_2$ (0.044 g, 39%) suitable for x-ray diffraction grew in 2 hours at -30°C. Anal. calcd. for $\text{CoC}_{50}\text{H}_{66}\text{Si}_6\text{O}_6$: C, 60.63; H, 6.72. Found: C, 60.98; H, 6.84.

Synthesis of $\text{Co}(\text{C}(\text{SiMe}_2\text{OC}_{10}\text{H}_7)_3)_2$ (**1**)

Solid CoBr_2 (41.6 mg, 0.190 mmol) was added to a stirring THF (8 ml) solution of $\text{KC}(\text{SiMe}_2\text{OC}_{10}\text{H}_7)_3$ (249 mg, 0.380 mmol) at room temperature. The reaction mixture was stirred for 4 hours at 60°C,

after which time the solution had turned green. The reaction mixture was filtered through diatomaceous earth, and solvent was removed under reduced pressure, leaving a green solid. The green solid was dissolved in hexanes (20 ml) and filtered to give an emerald green solution, from which brown-red crystals of **1** (17.8 mg, 7%) suitable for x-ray diffraction grew over the course of 3 days. Compound **1** is insoluble in all common organic solvents except THF, in which it forms a green solution. Anal. calcd. for $\text{CoC}_{74}\text{H}_{78}\text{O}_6\text{Si}_6$: C, 68.85; H, 6.09. Found: C, 68.36; H, 6.03.

Cooling the green hexanes solution appears to favor precipitation of the THF solvate, $\text{Co}(\text{C}(\text{SiMe}_2\text{OC}_{10}\text{H}_7)_3)_2(\text{THF})$. Green crystals not suitable for single-crystal x-ray diffraction were grown from the green hexanes solution over 1 day at -30°C, collected by filtration, and thoroughly dried in vacuo. Anal. calcd. for $\text{CoC}_{78}\text{H}_{86}\text{O}_7\text{Si}_6$: C, 68.74; H, 6.36. Found: C, 68.66; H, 6.52.

Synthesis of $\text{Zn}(\text{C}(\text{SiMe}_2\text{OC}_{10}\text{H}_7)_3)_2$ (**2**)

At room temperature, a solution of ZnBr_2 (35.1 mg, 0.155 mmol) dissolved in THF (2 ml) was added to a solution of $\text{KC}(\text{SiMe}_2\text{OC}_{10}\text{H}_7)_3$ (206 mg,

0.314 mmol) dissolved in THF (8 ml), and the mixture was stirred at room temperature for 12 hours. The reaction mixture was subsequently filtered through diatomaceous earth, and the THF solvent was removed under reduced pressure, leaving a white solid. The colorless solid was stirred in hexanes (20 ml) and filtered to give a pale-yellow solution, from which colorless crystals of **1** (36.7 mg, 9%) suitable for x-ray diffraction grew over the course of 1 day. Anal. calcd. for $\text{ZnC}_{74}\text{H}_{78}\text{O}_6\text{Si}_6$: C, 68.51; H, 6.06. Found: C, 68.14; H, 5.92.

Synthesis of $\text{Co}_{0.02}\text{Zn}_{0.98}(\text{C}(\text{SiMe}_2\text{OC}_{10}\text{H}_7)_3)_2$ (**3**)

Initially, $\text{CoBr}_2(\text{THF})$ was prepared by dissolving CoBr_2 (6.2 mg, 0.028 mmol) in THF (5 ml) and then removing the solvent under reduced pressure. A suspension of $\text{CoBr}_2(\text{THF})$ (0.028 mmol) and ZnBr_2 (57.4 mg, 25.5 mmol) was prepared in Et_2O (4 ml), and this suspension was added to a stirring solution of $\text{KC}(\text{SiMe}_2\text{OC}_{10}\text{H}_7)_3$ (371 mg, 0.567 mmol) dissolved in Et_2O (6 ml). The mixture was stirred for 1 hour at room temperature and then filtered through diatomaceous earth. A light pink powder was collected from the

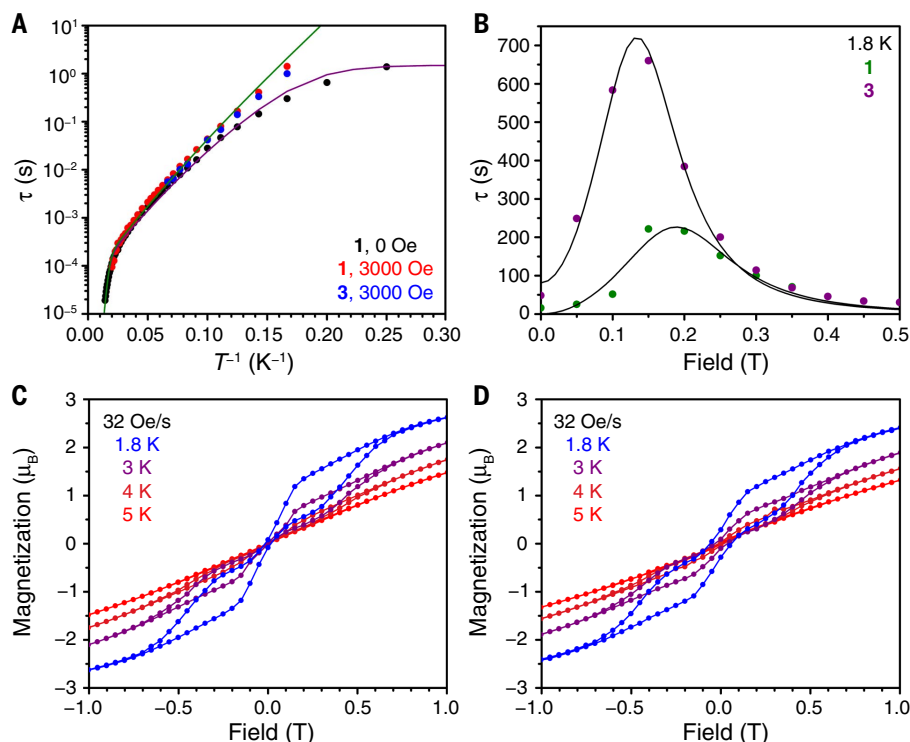


Fig. 5. Magnetic relaxation dynamics. (A) Arrhenius plot showing the natural log of relaxation time, τ , versus inverse temperature for **1** in the absence of an applied dc field (black circles), **1** under a 3000-Oe dc field (red circles), and **3** in the absence of an applied dc field (blue circles). Relaxation times are determined from fits of ac susceptibility measurements over the temperature range of 4 to 70 K. The purple and green lines represent fits of the relaxation data for **1** under 0 and 3000 Oe, respectively. (B) dc relaxation and magnetization times for **1** (green circles) and **3** (purple circles). The solid lines are from fits describing relaxation via tunneling and direct relaxation processes as described in the text and methods. (C) Variable-field magnetization data for **1** collected at temperatures ranging from 1.8 to 5 K at a field sweep rate of 32 Oe/s. (D) Variable-field magnetization data for **3** collected at temperatures ranging from 1.8 to 5 K at a field sweep rate of 32 Oe/s.

reaction mixture and the resulting light green Et₂O filtrate was put in a 20-ml vial. Crystallization tubes were added to the vial to increase the amount of crystallization surfaces, and Et₂O was added to fill the vial. Light pink crystals of **3** (63.9 mg, 9%) suitable for x-ray diffraction grew over the course of 4 days. Successful dilution was confirmed by determination of a unit cell consistent with pure **1** and **2**, and the metal composition was determined from comparison of molar magnetization data for the pure and diluted samples.

Single-crystal x-ray diffraction

In an argon-filled glove box, crystals of Co(C(SiMe₂OPh))₃, **1**, **2**, and **3** were coated in Paratone-N oil in individual vials, which were then sealed and remained sealed until immediately prior to mounting. Crystals were mounted on Kapton loops and cooled under a stream of N₂. Data were collected using a Bruker QUAZAR diffractometer equipped with a Bruker MICROSTAR x-ray source of Mo K α radiation (λ = 0.71073 Å) and an APEX-II detector. Raw data were integrated and corrected for Lorentz and polarization effects by using Bruker Apex3 v. 2016.5. Absorption corrections were applied by using SADABS (46). The space group was determined by examination of systematic absences, analysis of E-statistics, and successive refinement of the structure. The crystal structure was solved with ShelXT (47) and further refined with ShelXL (48) operated in the Olex2 software (49). The crystal did not show any substantial decay during data collection. Thermal parameters were refined anisotropically for all nonhydrogen atoms. Hydrogen atoms were placed in ideal positions and refined by using a riding model for all structures. A checkCIF report for **1** gave rise to a B-level alert regarding the ratio of maximum/minimum residual density. The maximum residual density for **1** lies in the naphthyl ring. In the case of the low-temperature synchrotron data used for CD modeling, disorder in the naphthyl ring was successfully modeled. For the data collected at 100 K used for the generation of the CIFs for **1** and **2**, we were unable to fully model this disorder; however, it is likely that the same disorder is responsible for the relatively large residual density.

UV-vis near-IR diffuse reflectance

UV-vis near-IR diffuse reflectance spectra were collected by using a CARY 5000 spectrophotometer interfaced with Varian Win UV software. The samples were prepared in a glove box and held in a Praying Mantis air-free diffuse reflectance cell. Powdered BaCO₃ was used as a nonabsorbing matrix. The spectra were collected in $F(R)$ versus wave number, where $F(R)$ is the Kubelka-Munk conversion $F(R) = (1 - R)^2/2R$ and R is reflectance.

Magnetometry

All magnetic measurements were carried out by using a Quantum Design MPMS-XL SQUID magnetometer, with the exception of those for the high-frequency ac magnetic susceptibility

data. High-frequency data (up to 10,000 Hz) were collected at the Quantum Design facility in San Diego, CA, by using a 9T PPMS instrument equipped with the ACSII measurement option to probe the ac moment at frequencies above 1000 Hz. For the measurements using the MPMS instrument, polycrystalline samples of **1** (32.1 mg) and **3** (49.7 mg) were loaded into quartz tubes (5 mm i.d., 7 mm o.d.) with a raised quartz platform. Solid eicosane was then added on top of the samples (32.0 and 61.2, respectively) to prevent crystallite torqueing and provide good thermal contact between the sample and the cryogenic bath. The tubes were fitted with Teflon sealable adapters, evacuated by using a glove box vacuum pump, and sealed under static vacuum by using an H₂/O₂ flame. Following flame sealing, the solid eicosane was melted in a water bath held at 40°C. When not in the magnetometer, the sealed samples were stored at -30°C. dc magnetic susceptibility data were collected for each sample from 2 to 300 K under dc fields ranging from 0 to 7 T. ac magnetic susceptibility data collected by using the MPMS instrument were obtained by using a 6-Oe switching field; data from the PPMS instrument were collected by using a 10-Oe switching field. All data were corrected for diamagnetic contributions of the eicosane and the individual samples by using Pascal's constants (50).

The ac susceptibility data were fit by using a generalized Debye model, which accounts for relaxation time (τ), attempt time (τ_0), isothermal susceptibility (χ_T), adiabatic susceptibility (χ_S), and the presence of a distribution of relaxation times (α) (51). Data for **1** collected under zero applied field and below 7 K exhibited high-frequency shoulders in χ'' , and fits to the data yielded very large α values, suggesting that a second, faster relaxation process might be operating at low temperatures. This second process may be related to the disordered molecules in the crystal. Data from 4 to 10 K were fit with two relaxation processes. Once the minor relaxation process moved out of the frequency range of the magnetometer (0.1 to 1488 Hz), a one-process fit was sufficient. The two fitting procedures gave only modestly different τ values for the 4 and 5 K data. The data for **3** and the applied-field data for **1** were fit sufficiently well with one process. Data collected by using the PPMS instrument (50 to 70 K, 100 to 10,000 Hz) gave some negative values for χ' at high frequency. Presumably, this result is due to the fact that the PPMS sample consisted of less material (6.9 mg of **1**, 29.0 mg of eicosane) and, especially at high temperatures, exhibited a smaller paramagnetic response relative to the diamagnetic response. The negative values did not affect the extraction of relaxation times, however. The method for fitting the relaxation data from 4 to 70 K is given in detail in the supplementary materials.

dc relaxation measurements were implemented with the hysteresis mode of the MPMS magnetometer by using small magnetizing fields such that the time to set the field was in the 10- to 30-s range; measurements were made every ~4 s.

We found that the relaxation times had a small dependence on the magnetizing field for **1** and a larger dependence for **3** (tables S19 and S20); the times reported in the main text are averages of those times. The relaxation times were determined by using a stretched exponential of the form $M_t = M_0 \exp[-(t/\tau)^n]$, where M_0 is the magnetization of the first data point measured, once the field was set, and n is a free variable (52).

dc magnetization experiments were implemented by applying a field to a sample at zero magnetization and measuring the magnetization until it became constant. Relaxation times were determined by using the equation $M_t = M_{\text{sat}} - (M_{\text{sat}} - M_0) \exp[-(t/\tau)^n]$, where M_{sat} is the saturation magnetization, M_0 is the magnetization of the first data point measured once the field was set, and n is a free variable. Magnetization times for **1** and **3** for each field are given in tables S20 and S21; the main text reports the average of these values (16.4 and 48.2 s, respectively) and their SD (0.7 and 4.7, respectively).

Variable-field FIR spectroscopy

FIR spectra were recorded on a Bruker IFS 66v/s FTIR spectrometer with a globar source and a composite bolometer detector element located inside an 11 T magnet directly below the sample. Approximately 5 mg of **1** was diluted in eicosane (1:10 ratio) and pressed in the shape of a 5-mm pellet. The sample was prepared and measured under an inert atmosphere. The sample was cooled to 4.2 K and irradiated with FIR light. Transmission spectra were recorded both in the absence and in the presence of a magnetic field (0 to 11 T).

CD modeling

Crystals of **1** are rather air sensitive, and thus all crystal manipulation was carried out inside of a glove box under an Ar atmosphere. A triangularly shaped single crystal with a maximum dimension of 0.10 mm was selected, and it was mounted by using cryo-protecting oil on a precentered glass fiber and then rapidly inserted into a cold He stream with a temperature of 20 K to minimize any risk of air exposure and subsequent crystal decay.

The crystal was mounted on the goniometer of beamline BL02B1 at the SPring8 synchrotron in Japan. The x-ray energy was fixed to 40 keV, corresponding to a wavelength of 0.30988 Å. We have previously experienced substantial crystal decay due to radiation damage, and this high energy was chosen in an attempt to avoid this detrimental effect. As shown in fig. S17, the frame scale factor, which accurately captures any crystal decay (as well as other systematic effects, such as beam intensity fluctuations), is scattered relatively close to 1.0 and does not drop off systematically, indicating that there is no substantial crystal decay.

The data were collected on a Fuji IP system by using 36 ω -scans with a width of 5° and an overlap of 0.5° for a total of 180° with a scan speed of 1 min/degree. Given the high symmetry of the compound, this protocol provided a complete dataset with sufficient redundancy. The

diffraction data ceased to be significant already at $\sin(\theta)/\lambda = 0.9 \text{ \AA}^{-1}$. As we explain below, there is substantial dynamic disorder in the crystal structure, which likely results in the lack of high-angle data.

The diffraction data were integrated by using dedicated Rigaku software RAPID AUTO v2.41, which integrates only the intensity of reflections estimated to be fully present on one frame, i.e., having been rotated fully through the Ewald sphere during one of the 5° rotations. This estimation obviously depends on the mosaicity of the crystal and the desired box size for integration. We experimented with these values in order to optimize the integration results, and those presented herein used mosaicity of 0.7° and a box size of 13×13 pixels. The raw images were scaled to accommodate the different sensitivities of the photomultiplier tubes, an effect which was uncovered in the summer of 2018.

The integration and subsequent scaling in RAPID AUTO provided a total of 43,260 reflections, which were then averaged by using the point group symmetry $\bar{3}$. These averaged data were reduced to 9008 unique reflections with an average redundancy of 4.8 and a completeness of 99.5% by using the program SORTAV. During refinement, it was noticed that the ratio of $F(\text{obs})$ to $F(\text{calc})$ varied systematically, and thus we decided to include 10 resolution-dependent scale factors that helped to alleviate this problem, as shown in fig. S19.

These data were used to solve the crystal structure by using SHELXT within the Olex2 interface. The structure solution was found to contain a minor, but clearly visible, disordered component, and the disorder is solely in the naphthalene moiety (see fig. S18). The disorder is perhaps best explained as resulting from a mirror symmetry in the plane defined by C(1) (bonded to Co) and partially by Si(1) and O(1). This plane also very nearly includes C(2) [carbon bonded to O(1)]. The occupation of the disordered parts is 4.8%, and including this disorder in the model leads to a substantial improvement of the refinement.

Despite the substantial disorder (one of the consequences of which is that some atoms in the structure are nearly overlapping), we decided to attempt multipole-based CD modeling. The independent-atom model (IAM) structure from ShelX was exported to the program XD, which is based on the Hansen-Coppens multipole formalism. Herein, we kept the extent of disorder fixed on the values obtained from ShelX and furthermore used isotropic thermal parameters for the disordered atoms. We did not apply multipole parameters to the disordered atoms, which were kept spherical. Given the nearly whole-molecule disorder, it is imperative to be extremely careful during the refinement procedure. Thus, we used constraints to avoid overfitting, which otherwise is a possibility in such a disordered system. The use of isotropic and spherical disordered atoms helps with this as well.

The final multipole model consists of hexadecapoles on Co and octopoles on all other non-H

atoms (except the disordered atoms), whereas H atoms were refined by using one common monopole and bond-directed dipole. The model was reached after several refinements, in which the level of multipoles was increased by one for each step. Both neutral and ionic scattering factors were tested for Co. In the final model, a neutral scattering factor was used.

In the final refinement, the largest residuals were, as expected, near the Si and the Co atoms. The largest residuals were positive [the largest is around 1.2 e\AA^{-3} (where e\AA^{-3} is electrons per cubic angstrom) and is close to the Co] and notably larger than the most negative residual density peaks, which were around -0.55 e\AA^{-3} . Such large discrepancy between the positive and negative residuals may indicate that the disorder was not fully accounted for. The Co atom sits on a special position in the space group with a multiplicity of 6, and it is possible that the high residual density at this position is also a result of this high symmetry. The residual near Co does not indicate that the atom sits off-centered. However, it may be related to the disorder, and perhaps it does not sit in a harmonic potential. We tried to refine anharmonic thermal parameters, but this refinement had no effect on the residual density.

The residual density distribution, interpreted by using the fractal dimensionality plots as first presented by Meindl and Henn (fig. S19) (53), shows a somewhat distorted parabola, with a slight tendency to increase more toward the positive residuals. However, this increase is much smaller than expected from the substantial residuals near Co and Si and suggests that despite the disorder, the multipole model may be quantitatively useful.

Co sits on a $\bar{3}$ crystallographic position, and therefore only four multipole parameters are symmetry-allowed. The most important parameter in this respect is the quadrupole along the z axis. However, in the least-squares refinement, this parameter correlates strongly with the thermal parameters, including U33, which represents the atomic vibration along the same z direction. To avoid this correlation, we separated the refinement of multipole parameters from the refinement of atomic positions and vibrations. We first attempted a high-angle refinement of the atomic vibrations and positions, but the resulting refinement of multipole parameters led to unphysical values—for instance, atomic charges derived from monopole values of more than +2 and κ -parameters deviating by more than 20% from unity. Instead, we chose to use the full dataset to independently refine the atomic positions and vibrations of all atoms, subsequently fixing these values and refining the multipole parameters until convergence. This approach represented the final model, from which we extracted the d-orbital population ratios. In the final model, the charge on Co was determined to be +1.3.

REFERENCES AND NOTES

1. I. G. Rau *et al.*, Reaching the magnetic anisotropy limit of a 3d metal atom. *Science* **344**, 988–992 (2014). doi: [10.1126/science.1252841](https://doi.org/10.1126/science.1252841); pmid: [24812206](https://pubmed.ncbi.nlm.nih.gov/24812206/)

2. W. M. Reiff, A. M. LaPointe, E. H. Witten, Virtual free ion magnetism and the absence of Jahn-Teller distortion in a linear two-coordinate complex of high-spin iron(II). *J. Am. Chem. Soc.* **126**, 10206–10207 (2004). doi: [10.1021/ja030632w](https://doi.org/10.1021/ja030632w); pmid: [15315408](https://pubmed.ncbi.nlm.nih.gov/15315408/)
3. J. M. Zadrozny *et al.*, Slow magnetization dynamics in a series of two-coordinate iron(II) complexes. *Chem. Sci.* **4**, 125–138 (2013). doi: [10.1039/C2SC20801F](https://doi.org/10.1039/C2SC20801F)
4. J. M. Zadrozny *et al.*, Magnetic blocking in a linear iron(I) complex. *Nat. Chem.* **5**, 577–581 (2013). doi: [10.1038/nchem.1630](https://doi.org/10.1038/nchem.1630); pmid: [23787747](https://pubmed.ncbi.nlm.nih.gov/23787747/)
5. D. Gatteschi, R. Sessoli, J. Villain, *Molecular Nanomagnets* (Oxford Univ. Press, 2006).
6. J. M. Zadrozny *et al.*, Mössbauer spectroscopy as a probe of magnetization dynamics in the linear iron(I) and iron(II) complexes $[\text{Fe}(\text{C}(\text{SiMe}_3)_3)_2]^{1-0}$. *Inorg. Chem.* **52**, 13123–13131 (2013). doi: [10.1021/ic402013n](https://doi.org/10.1021/ic402013n); pmid: [24175913](https://pubmed.ncbi.nlm.nih.gov/24175913/)
7. M. Atanasov, J. M. Zadrozny, J. R. Long, F. Neese, A theoretical analysis of chemical bonding, vibronic coupling, and magnetic anisotropy in linear iron(II) complexes with single-molecule magnet behavior. *Chem. Sci.* **4**, 139–156 (2013). doi: [10.1039/C2SC21394J](https://doi.org/10.1039/C2SC21394J)
8. The term “spin-reversal barrier” is somewhat ambiguous in the single-molecule magnet literature. In the systems described here, we define it as the separation between ground and first excited M_J (or M_S) states. Thus, “over-barrier” relaxation refers to excitation from $M_J = +J$ to $M_J = +(J-1)$ states followed by relaxation to the $M_J = -J$ state (an Orbach mechanism). “Through-barrier” relaxation mechanisms are any that allow the system to go from $M_J = +J$ to $M_J = -J$ without excitation to the $M_J = +(J-1)$ state.
9. M. Atanasov *et al.*, First principles approach to the electronic structure, magnetic anisotropy and spin relaxation in mononuclear 3d-transition metal single molecule magnets. *Coord. Chem. Rev.* **289–290**, 177–214 (2015). doi: [10.1016/j.ccr.2014.10.015](https://doi.org/10.1016/j.ccr.2014.10.015)
10. P. Zhao *et al.*, Synthesis and structural characterization of a dimeric cobalt(I) homoleptic alkyl and an iron(II) alkyl halide complex. *Organometallics* **33**, 1917–1920 (2014). doi: [10.1021/om500180u](https://doi.org/10.1021/om500180u)
11. P. P. Power, Stable two-coordinate, open-shell (d^1-d^9) transition metal complexes. *Chem. Rev.* **112**, 3482–3507 (2012). doi: [10.1021/cr2004647](https://doi.org/10.1021/cr2004647); pmid: [22480221](https://pubmed.ncbi.nlm.nih.gov/22480221/)
12. T. Viehhaus, W. Schwarz, K. Hübner, K. Locke, J. Weidlein, Das unterschiedliche Reaktionsverhalten von basefreiem Tris(trimethylsilyl)methyl-Lithium gegenüber den Trihalogeniden der Erdmetalle und des Eisens. *Z. Anorg. Allg. Chem.* **627**, 715 (2001). doi: [10.1002/1521-3749\(200104\)627:4<715::AID-ZAAC715>3.0.CO;2-O](https://doi.org/10.1002/1521-3749(200104)627:4<715::AID-ZAAC715>3.0.CO;2-O)
13. N. H. Buttrus, C. Eaborn, P. B. Hitchcock, J. D. Smith, A. C. Sullivan, Preparation and crystal structure of a two-coordinate manganese compound, bis(tris(trimethyl)silylmethyl)manganese. *J. Chem. Soc. Chem. Commun.* **1985**, 1380–1381 (1985). doi: [10.1039/c39850001380](https://doi.org/10.1039/c39850001380)
14. C.-Y. Lin *et al.*, Salts of the two-coordinate homoleptic manganese(II) dialkyl anion $[\text{Mn}(\text{C}(\text{SiMe}_3)_3)_2]^-$ with quenched orbital magnetism. *Chem. Commun.* **51**, 13275–13278 (2015). doi: [10.1039/C5CC005166E](https://doi.org/10.1039/C5CC005166E); pmid: [26178861](https://pubmed.ncbi.nlm.nih.gov/26178861/)
15. X.-N. Yao *et al.*, Two-coordinate Co(II) imido complexes as outstanding single-molecule magnets. *J. Am. Chem. Soc.* **139**, 373–380 (2017). doi: [10.1021/jacs.6b11043](https://doi.org/10.1021/jacs.6b11043); pmid: [27936686](https://pubmed.ncbi.nlm.nih.gov/27936686/)
16. P. E. Kazin *et al.*, A Co-based single-molecule magnet confined in a barium phosphate apatite matrix with a high energy barrier for magnetization relaxation. *Chem. Commun.* **53**, 5416–5419 (2017). doi: [10.1039/C7CC02453C](https://doi.org/10.1039/C7CC02453C); pmid: [28453011](https://pubmed.ncbi.nlm.nih.gov/28453011/)
17. H. Li *et al.*, A zwitterionic carbanion frustrated by boranes—dihydrogen cleavage with weak Lewis acids via an “inverse” frustrated Lewis pair approach. *J. Am. Chem. Soc.* **135**, 16066–16069 (2013). doi: [10.1021/ja409330h](https://doi.org/10.1021/ja409330h); pmid: [24124979](https://pubmed.ncbi.nlm.nih.gov/24124979/)
18. H. Li, A. J. Aquino, D. B. Cordes, W. L. Hase, C. Krepner, Electronic nature of zwitterionic alkali metal methanides, silanides, and germanides—a combined experimental and computational approach. *Chem. Sci.* **8**, 1316–1328 (2017). doi: [10.1039/c6sc02390h](https://doi.org/10.1039/c6sc02390h)
19. S. S. Al-Juaid *et al.*, The preparation and crystal structures of the compounds $(\text{Ph}_2\text{MeSi})_3\text{CMCl}$ (M = Zn, Cd, or Hg). *J. Organomet. Chem.* **462**, 45–55 (1993). doi: [10.1016/0022-328X\(93\)83340-2](https://doi.org/10.1016/0022-328X(93)83340-2)
20. S. S. Al-Juaid *et al.*, Tris(triorganosilyl)methyl derivatives of potassium and lithium bearing dimethylamino or methoxy

- substituents at silicon. Crystal structures of $\text{K}(\text{SiMe}_3)_2$ ($\text{SiMe}_2\text{NMe}_2$), $\text{K}(\text{SiMe}_2\text{NMe}_2)_3$ and $[\text{Li}(\text{SiMe}_3)(\text{SiMe}_2\text{OMe})_2]_2$. *J. Chem. Soc. Dalton Trans.* **1999**, 3267–3273 (1999). doi: [10.1039/a904043i](https://doi.org/10.1039/a904043i)
21. M. Westerhausen, B. Rademacher, W. Poll, Trimethylsilyl-substituierte Derivate des Dimethylzinks—Synthese, spektroskopische Charakterisierung und Struktur. *J. Organomet. Chem.* **421**, 175–188 (1991). doi: [10.1016/0022-328X\(91\)86402-C](https://doi.org/10.1016/0022-328X(91)86402-C)
 22. M. Nishio, The CH/ π hydrogen bond in chemistry. Conformation, supramolecules, optical resolution and interactions involving carbohydrates. *Phys. Chem. Chem. Phys.* **13**, 13873–13900 (2011). doi: [10.1039/c1cp20404a](https://doi.org/10.1039/c1cp20404a); pmid: [21611676](https://pubmed.ncbi.nlm.nih.gov/21611676/)
 23. C.-Y. Lin *et al.*, Dispersion force stabilized two-coordinate transition metal–amido complexes of the $-\text{N}(\text{SiMe}_3)\text{Dipp}$ ($\text{Dipp} = \text{C}_6\text{H}_3-2,6\text{-Pr}_2$) ligand: Structural, spectroscopic, magnetic, and computational studies. *Inorg. Chem.* **52**, 13584–13593 (2013). doi: [10.1021/ic402105m](https://doi.org/10.1021/ic402105m)
 24. A. J. Wallace, B. E. Williamson, D. L. Crittenden, CASSCF-based explicit ligand field models clarify the ground state electronic structures of transition metal phthalocyanines (MPC; M = Mn, Fe, Co, Ni, Cu, Zn). *Can. J. Chem.* **94**, 1163–1168 (2016). doi: [10.1139/cjc-2016-0264](https://doi.org/10.1139/cjc-2016-0264)
 25. R. F. W. Bader, *Atoms in Molecules: A Quantum Theory* (Clarendon Press, 1990).
 26. R. Marx *et al.*, Spectroscopic determination of crystal field splittings in lanthanide double deckers. *Chem. Sci.* **5**, 3287–3293 (2014). doi: [10.1039/c4sc00751d](https://doi.org/10.1039/c4sc00751d)
 27. Y. Rechkemmer *et al.*, A four-coordinate cobalt(II) single-ion magnet with coercivity and a very high energy barrier. *Nat. Commun.* **7**, 10467 (2016). doi: [10.1038/ncomms10467](https://doi.org/10.1038/ncomms10467); pmid: [26883902](https://pubmed.ncbi.nlm.nih.gov/26883902/)
 28. D. Gatteschi, R. Sessoli, Quantum tunneling of magnetization and related phenomena in molecular materials. *Angew. Chem. Int. Ed.* **42**, 268–297 (2003). doi: [10.1002/anie.200390099](https://doi.org/10.1002/anie.200390099); pmid: [12548682](https://pubmed.ncbi.nlm.nih.gov/12548682/)
 29. K. N. Shrivastava, Theory of spin-lattice relaxation. *Phys. Status Solidi B* **117**, 437–458 (1983). doi: [10.1002/pssb.2221170202](https://doi.org/10.1002/pssb.2221170202)
 30. R. Orbach, Spin-lattice relaxation in rare-earth salts. *Proc. R. Soc. London Ser. A* **264**, 458 (1961).
 31. A. Lunghi, F. Totti, R. Sessoli, S. Sanvito, The role of anharmonic phonons in under-barrier spin relaxation of single molecule magnets. *Nat. Commun.* **8**, 14620 (2017). doi: [10.1038/ncomms14620](https://doi.org/10.1038/ncomms14620); pmid: [28262663](https://pubmed.ncbi.nlm.nih.gov/28262663/)
 32. A. Lunghi, F. Totti, S. Sanvito, R. Sessoli, Intra-molecular origin of the spin-phonon coupling in slow-relaxing molecular magnets. *Chem. Sci.* **8**, 6051–6059 (2017). doi: [10.1039/C7SC02832F](https://doi.org/10.1039/C7SC02832F); pmid: [28989635](https://pubmed.ncbi.nlm.nih.gov/28989635/)
 33. S.-D. Jiang, B.-W. Wang, G. Su, Z.-M. Wang, S. Gao, A mononuclear dysprosium complex featuring single-molecule-magnet behavior. *Angew. Chem. Int. Ed.* **49**, 7448–7451 (2010). doi: [10.1002/anie.201004027](https://doi.org/10.1002/anie.201004027); pmid: [20803599](https://pubmed.ncbi.nlm.nih.gov/20803599/)
 34. H. A. Kramers, A general theory of paramagnetic rotation in crystals. *Proc. R. Acad. Sci. Amsterdam* **33**, 959 (1930).
 35. M. Gönidec, E. S. Davies, J. McMaster, D. B. Amabilino, J. Veciana, Probing the magnetic properties of three interconvertible redox states of a single-molecule magnet with magnetic circular dichroism spectroscopy. *J. Am. Chem. Soc.* **132**, 1756–1757 (2010). doi: [10.1021/ja9095895](https://doi.org/10.1021/ja9095895); pmid: [20099818](https://pubmed.ncbi.nlm.nih.gov/20099818/)
 36. L. Margheriti *et al.*, X-ray detected magnetic hysteresis of thermally evaporated terbium double-decker oriented films. *Adv. Mater.* **22**, 5488–5493 (2010). doi: [10.1002/adma.201003275](https://doi.org/10.1002/adma.201003275); pmid: [20949539](https://pubmed.ncbi.nlm.nih.gov/20949539/)
 37. M. Gönidec *et al.*, Surface supramolecular organization of a terbium(III) double-decker complex on graphite and its single molecule magnet behavior. *J. Am. Chem. Soc.* **133**, 6603–6612 (2011). doi: [10.1021/ja109296c](https://doi.org/10.1021/ja109296c); pmid: [21486019](https://pubmed.ncbi.nlm.nih.gov/21486019/)
 38. D. Klar *et al.*, Hysteretic behaviour in a vacuum deposited submonolayer of single ion magnets. *Dalton Trans.* **43**, 10686–10689 (2014). doi: [10.1039/C4DT01005A](https://doi.org/10.1039/C4DT01005A); pmid: [24875369](https://pubmed.ncbi.nlm.nih.gov/24875369/)
 39. M. Mannini *et al.*, Magnetic behaviour of TbPc_2 single-molecule magnets chemically grafted on silicon surface. *Nat. Commun.* **5**, 4582 (2014). doi: [10.1038/ncomms5582](https://doi.org/10.1038/ncomms5582); pmid: [25109254](https://pubmed.ncbi.nlm.nih.gov/25109254/)
 40. J. Dreiser *et al.*, Exchange interaction of strongly anisotropic tripodal erbium single-ion magnets with metallic surfaces. *ACS Nano* **8**, 4662–4671 (2014). doi: [10.1021/nn500409u](https://doi.org/10.1021/nn500409u); pmid: [24645922](https://pubmed.ncbi.nlm.nih.gov/24645922/)
 41. C. Wäckerlin *et al.*, Giant hysteresis of single-molecule magnets adsorbed on a nonmagnetic insulator. *Adv. Mater.* **28**, 5195–5199 (2016). doi: [10.1002/adma.201506305](https://doi.org/10.1002/adma.201506305); pmid: [27159732](https://pubmed.ncbi.nlm.nih.gov/27159732/)
 42. M. Getzlaff, *Fundamentals of Magnetism* (Springer-Verlag, 2008).
 43. A. Jesche *et al.*, Giant magnetic anisotropy and tunnelling of the magnetization in $\text{Li}_2(\text{Li}_{1-x}\text{Fe}_x)\text{N}$. *Nat. Commun.* **5**, 3333 (2014). doi: [10.1038/ncomms4333](https://doi.org/10.1038/ncomms4333); pmid: [24566374](https://pubmed.ncbi.nlm.nih.gov/24566374/)
 44. C. J. Schaverien, A. G. Orpen, Chemistry of (octaethylporphyrinato)lutetium and -yttrium complexes: Synthesis and reactivity of (OEP)MX derivatives and the selective activation of O_2 by (OEP)Y(μ -Me) $_2\text{AlMe}_2$. *Inorg. Chem.* **30**, 4968–4978 (1991). doi: [10.1021/ic00026a023](https://doi.org/10.1021/ic00026a023)
 45. K. D. Safa, S. Tofangdarzadeh, H. H. Ayenaddeh, Reactions of tris(dimethylsilyl)methane and polymers containing Si–H groups with various hydroxy compounds under aerobic and mild conditions. *Heteroatom Chem.* **19**, 365–376 (2008). doi: [10.1002/hc.20440](https://doi.org/10.1002/hc.20440)
 46. G. M. Sheldrick, SADABS, version 2.03 (Bruker Analytical X-Ray Systems, 2000).
 47. G. M. Sheldrick, SHELXT – integrated space-group and crystal-structure determination. *Acta Crystallogr. A* **71**, 3–8 (2015). doi: [10.1107/S2053273314026370](https://doi.org/10.1107/S2053273314026370); pmid: [25537383](https://pubmed.ncbi.nlm.nih.gov/25537383/)
 48. G. M. Sheldrick, Crystal structure refinement with SHELXL. *Acta Crystallogr. C* **71**, 3–8 (2015). doi: [10.1107/S0108767307043930](https://doi.org/10.1107/S0108767307043930); pmid: [25567568](https://pubmed.ncbi.nlm.nih.gov/25567568/)
 49. O. V. Dolomanov, L. J. Bourhis, R. J. Gildea, J. A. K. Howard, H. Puschmann, OLEX2: A complete structure solution, refinement and analysis program. *J. Appl. Crystallogr.* **42**, 339–341 (2009). doi: [10.1107/S0021889808042726](https://doi.org/10.1107/S0021889808042726)
 50. G. A. Bain, J. F. Berry, Diamagnetic corrections and Pascal's constants. *J. Chem. Educ.* **85**, 532 (2008). doi: [10.1021/ed085p532](https://doi.org/10.1021/ed085p532)
 51. K. S. Cole, R. H. Cole, Dispersion and absorption in dielectrics I. Alternating current characteristics. *J. Chem. Phys.* **9**, 341–351 (1941). doi: [10.1063/1.1750906](https://doi.org/10.1063/1.1750906)
 52. C. Sangregorio, T. Ohm, C. Paulsen, R. Sessoli, D. Gatteschi, Quantum tunneling of the magnetization in an iron cluster nanomagnet. *Phys. Rev. Lett.* **78**, 4645–4648 (1997). doi: [10.1103/PhysRevLett.78.4645](https://doi.org/10.1103/PhysRevLett.78.4645)
 53. K. Meindl, J. Henn, Foundations of residual-density analysis. *Acta Crystallogr. A* **64**, 404–418 (2008). doi: [10.1107/S0108767308006879](https://doi.org/10.1107/S0108767308006879)

ACKNOWLEDGMENTS

We thank K. R. Meihaus for editorial assistance. **Funding:** This work was funded by NSF grant CHE-1464841 (P.C.B., J.R.L.), Max-Planck Gesellschaft (M.A., F.N.), DNR93 and Danscatt (E.D.-M., J.O.), and DFG SL104/5-1 (M.P., J.V.S.). **Author contributions:** Synthesis, magnetic characterization, and analysis were performed by P.C.B. and J.R.L. Ab initio calculations and analysis were performed by M.A. and F.N. Applied-field FIR spectra were collected and analyzed by M.P., I.C., M.O., and J.V.S. CD data collection and modeling were performed by E.D.-M. and J.O. **Competing interests:** The authors have no competing interests to claim. **Data and materials availability:** Crystallographic data for **1**, **2**, and $\text{Co}(\text{C}(\text{SiMe}_2\text{OPh})_3)_2$ are freely available from the Cambridge Crystallographic Data Centre under CCDC numbers 1872361, 1872361, and 1872363, respectively. The supplementary materials include details on the fitting of magnetic relaxation data, as well as computational methods.

SUPPLEMENTARY MATERIALS

www.sciencemag.org/content/362/6421/eaat7319/suppl/DC1
Materials and Methods
Figs. S1 to S19
Tables S1 to S22
References (54–70)

28 March 2018; resubmitted 2 August 2018
Accepted 1 November 2018
Published online 15 November 2018
[10.1126/science.aat7319](https://doi.org/10.1126/science.aat7319)

A linear cobalt(II) complex with maximal orbital angular momentum from a non-Aufbau ground state

Philip C. Bunting, Mihail Atanasov, Emil Damgaard-Møller, Mauro Perfetti, Iris Crassee, Milan Orlita, Jacob Overgaard, Joris van Slageren, Frank Neese and Jeffrey R. Long

Science **362** (6421), eaat7319.

DOI: 10.1126/science.aat7319 originally published online November 15, 2018

Cobalt unfettered by its ligand field

Applied magnetic fields induce a field in any compound with unpaired electrons. However, for the induced field to persist once the applied field is gone, the electrons must be configured to manifest orbital angular momentum. Generally, the influence of ligands severely restricts that property in transition metal complexes. Bunting *et al.* now show that a cobalt ion is just barely affected by two linearly coordinated carbon ligands and, as such, exhibits maximal orbital angular momentum. Although its magnetic properties mainly pertain at very low temperature, its structure offers a more general design principle.

Science, this issue p. eaat7319

ARTICLE TOOLS

<http://science.sciencemag.org/content/362/6421/eaat7319>

SUPPLEMENTARY MATERIALS

<http://science.sciencemag.org/content/suppl/2018/11/14/science.aat7319.DC1>

REFERENCES

This article cites 68 articles, 1 of which you can access for free
<http://science.sciencemag.org/content/362/6421/eaat7319#BIBL>

PERMISSIONS

<http://www.sciencemag.org/help/reprints-and-permissions>

Use of this article is subject to the [Terms of Service](#)